THE GEOLOGICAL SOCIETY OF AMERICA®

Lithosphere tearing and foundering during continental subduction: Insights from Oligocene–Miocene magmatism in southern Tibet

Fabin Pan[1,†], Hongfei Zhang[1,†], Xiaobo He[2,†], Nigel Harris[3], Hong-Kun Dai[1], Qing Xiong[1], Biji Luo[1], Dong Liu[4], Timothy Kusky[1], and Izhar Sadiq[1]

[1]*State Key Laboratory of Geological Processes and Mineral Resources, and School of Earth Science, China University of Geosciences, Wuhan 430074, P.R. China*

[2]*College of Marine Science and Technology, Zhejiang Ocean University, Zhoushan, P.R. China*

[3]*School of Environment, Earth and Ecosystem Sciences, The Open University, Milton Keynes MK7 6AA, UK*

[4]*State Key Laboratory of Geological Processes and Mineral Resources, and School of Earth Science and Resources, China University of Geosciences, Beijing 100083, P.R. China*

ABSTRACT

The distribution of Oligo–Miocene magmatic rocks from southern Tibet in space and time yields critical information on the geometry and deformation of the subducted Indian lithosphere which impacts on plateau growth following the India and Eurasia collision. A growing body of geophysical evidence has shown that the subducted Indian lithosphere beneath the Tibetan Plateau has been torn apart. However, the spatiotemporal distribution and cause of the tearing remain enigmatic. Timing of the post-collisional magmatic rocks in southern Tibet exhibits four patterns of decreasing ages; magmatism began earlier in the west and east Himalayan syntaxis and evolved to two age undulations in the central southern Tibet. Seismic images show that regions of slab window (both 90°E and 84°E) and flattened subducted lithosphere (both 86°E and 81°E) are present at depth of 135 km. Correspondingly, increasing mineral crystallization temperatures (absolute value of 50 °C) were recorded in the Oligo–Miocene ultrapotassic-potassic rocks at 90°E and 84°E, while opposing trends were shown by coeval ultrapotassic-potassic rocks at 86°E and 81°E. Besides, the melting depth of the Oligo–Miocene ultrapotassic-potassic primitive melts decreases from nearly 100 km to 70 km between 81°E and 90°E, probably indicating progressive rising of the lithosphere-asthenosphere boundary. Such variations were possibly the results of the focused flow and upwelling of asthenosphere, which advanced rapidly but diachronously through weakened and torn sectors within the overlying Indian slab. The upwellings probably induced diachronously upward bending of the residual Indian slab and its flattening, which accelerated the tearing of the Indian lithosphere during continental subduction.

INTRODUCTION

Widespread discovery of ultrahigh pressure rocks worldwide indicates that continental crust with positive buoyancy can be subducted to mantle depths (Gilotti, 2013; Lanari et al., 2013; Ye et al., 2000). Cenozoic continental subduction along the Alpine belt and the Himalayan belt is observed seismically (Gao et al., 2016; Kosarev et al., 1999; Shi et al., 2020; Zhao et al., 2015). However, the interplay between the downgoing continental slab and upwelling asthenosphere from below the slab is still enigmatic. Cenozoic collision between the Indian and Eurasian continents led to thickening and uplift of the Tibetan crust since ca. 55 Ma (Chung et al., 2005; Coulon et al., 1986; Molnar et al., 1993; Zhu et al., 2019), which offers a classic example of geodynamic processes during continental subduction, and a testing ground for deeper understanding of collisional processes.

Mantle seismic tomography on the geometry of the underthrusting Indian lithosphere is critical in deciphering the intrinsic relations between the continental collision and the rising plateau. The front of the subducted Indian lithosphere (SIL) has been suggested to extend as far as the Bangong-Nujiang suture in central Tibet (Kosarev et al., 1999; Tilmann et al., 2003). The downgoing Indian lithosphere was recently proposed to be fragmented by tearing at varying dip angles (Chen et al., 2015; Li and Song, 2018; Liang et al., 2016; Liu et al., 2020). Other studies suggest that a large portion of the Indian crust may either return to the surface via crustal-scale duplexing (Gao et al., 2016) and/or sink into the deep mantle (Shi et al., 2020) rather than underplate the base of the Asian lithosphere. Overall, geodynamic processes and their contributions to the Cenozoic deformation of the Tibetan Plateau remain the subject of much debate.

Fragmentation of the downgoing Indian lithosphere would permit or induce asthenospheric upwelling (Liang et al., 2016, Wang et al., 2022), resulting in partial melting of the overriding lithosphere. Asthenospheric materials filling the newly formed gap might cause decreasing melting depth and increasing magma temperature. Thus, the post-collisional (ca. 30–10 Ma) magmatism in southern Tibet provides potential proxies for recording the tearing processes of the Indian lithosphere as well as deciphering the driving force(s) for Cenozoic tectonism in the Tibetan Plateau. In this paper, we carry out an integrated study comprising zircon U-Pb dating and mineral chemistry from 8 ultrapotassic-potassic rocks in the central part of the Lhasa terrane and 14 felsic dykes in both the west Himalayan syntaxis (WHS) and the east Himalayan syntaxis (EHS) (Supplemental Data S1[1];

[†]panfabin@cug.edu.cn, hfzhang@cug.edu.cn, xiaobo.he@zjou.edu.cn

[1]Supplemental Material. Supplemental Data S1: Major and trace elements and age data summary of the studied Oligocene–Miocene magmatic rocks. Supplemental Data S2: Zircon trace elements of the studied Oligocene–Miocene magmatic rocks. Table S1: Zircon U-Pb ages of the studied Oligocene–Miocene magmatic rocks. Table S2: Clinopyroxene major elements of the studied Miocene ultrapotassic-potassic volcanic rocks. Table S3: Published ages of the Oligocene to Miocene magmatic rocks in southern Tibet. Table S4: Calculated primary magmas and pressure estimates of the ultrapotassic rocks in southern Tibet. Please visit https://doi.org/10.1130/GSAB.S.22088414 to access the supplemental material, and contact editing@geosociety.org with any questions.

GSA Bulletin; https://doi.org/10.1130/B36746.1; 12 figures; 1 supplemental file.

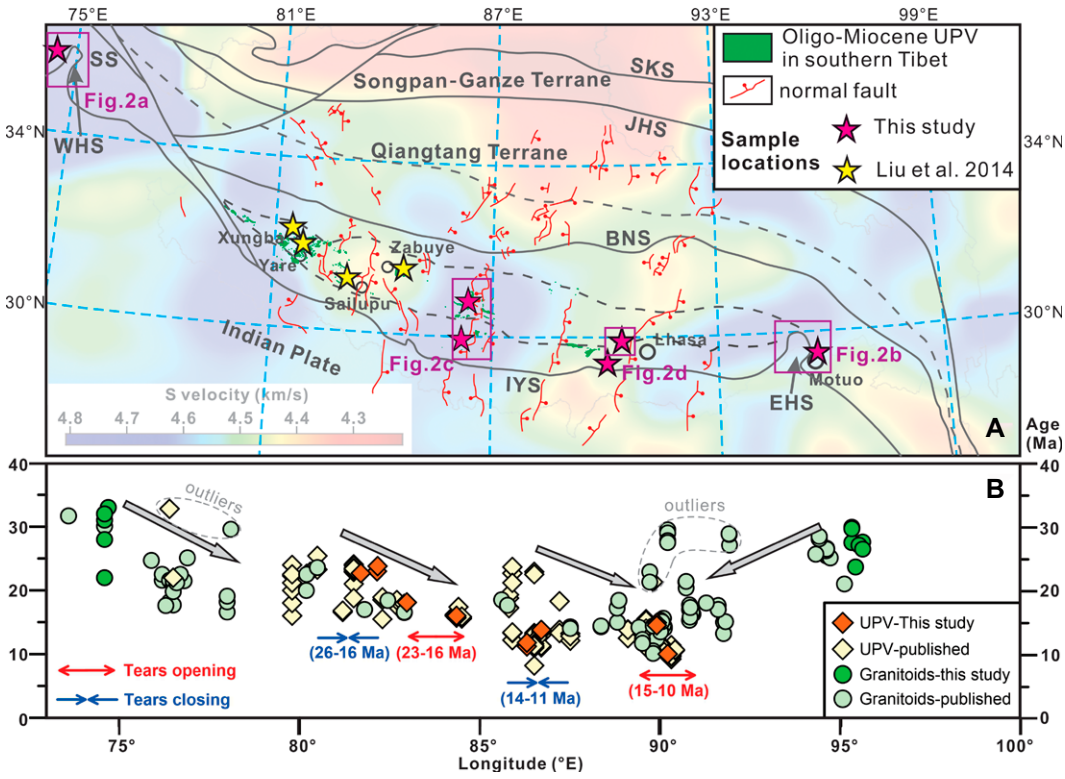

Figure 1. (A) Geological map and S-wave seismic velocity variations of the Tibetan Plateau and the adjacent regions at 135 km depth with emphasis on high and low zones along the Indus/Yarlung Tsangpo Suture zone (IYS) in southern Tibet (S-wave seismic image modified after Li and Song, 2018). The N-S–trending normal fault systems are according to Bian et al. (2021). SKS—South Kunlun suture; JHS—Jinsha-Honghe suture; BNS—Bangong-Nujiang suture; EHS—the east Himalayan syntaxis; SS—Shyok suture; UPV—ultrapotassic-potassic volcanics; WHS—the west Himalayan syntaxis. (B) Diachronous distribution of the post-collisional magmatism in southern Tibet. Age distribution model of Oligocene–Miocene magmatism shows four decreasing age trends. UPV—ultrapotassic-potassic volcanic rocks. Detailed data sources are present in Table S3.

Fig. 1). Together with the published age results (212 dated samples) of the post-collisional magmatic rocks in southern Tibet, our aims are: (1) to establish a detailed age spectrum from WHS and EHS toward the central region of the Lhasa terrane as well as to determine magma crystallization temperature variations in southern Tibet, and (2) to discuss the possible geodynamic coupling between tearing of the Indian lithosphere and upwelling deeper asthenosphere during continental collision.

GEOLOGICAL SETTING AND SAMPLES

The "Trans-Himalayan Batholith," which crops out north of the Indus-Yarlung Suture in southern Tibet, is dominantly composed of the Mesozoic-Cenozoic plutonic complex in the Kohistan and Ladakh island arc west of 80°E and the Lhasa terrane east of 80°E (Searle et al., 1987). The Late Cretaceous to Eocene (120–40 Ma) continental arc magmatic rocks in the Trans-Himalayan Batholith directly recorded subduction of the Neo-Tethyan Ocean slab before 55 Ma and then initiation of the following India-Asia collision (e.g., Chung et al., 2005; Zhu et al., 2019). Both the WHS and EHS mark the western and eastern extremities of the Himalayan orogen in southern Tibet, and are mapped as northward loops of the Indus-Yarlung Suture, indicating giant "pop-up" structures with Indian Precambrian basement core and the Trans-Himalayan Batholith margin (Figs. 1A, 2A, and 2B).

The post-collisional magmatic rocks in southern Tibet comprise ultrapotassic-potassic volcanics, mainly in the central and western parts of the Lhasa terrane (Fig. 1A), and calc-alkaline intrusions that are widespread but of small volume in the Trans-Himalayan Batholith. The distribution of these magmatic rocks is sometimes controlled by the N-S–trending normal fault systems in southern Tibet (Figs. 1A, 2C, and 2D). The ultrapotassic and low-silica potassic volcanics are commonly considered to be derived from the metasomatized lithospheric mantle beneath Tibet (Guo et al., 2015; Guo and Wilson, 2019; Hao et al., 2022; Mahéo et al., 2002; Miller et al., 1999; Nomade et al., 2004; Sun et al., 2018; Turner et al., 1996; Williams et al., 2004; Zhao et al., 2009), while the calc-alkaline intrusions have been suggested to be dominantly derived from the lower crust of the southern Lhasa terrane (Chung et al., 2003; Hao et al., 2021; Hou et al., 2004; Pan et a., 2012; Sun et al., 2018).

Detailed individual sample descriptions are shown in Supplemental Data S1. The potassic-ultrapotassic rocks in this study contain phonotephlite-trachyandesite and phonotephlite-trachyandesitic dykes with porphyritic textures (Figs. 3A–3K). Phenocrysts (20%–45%) for the phonotephlite-trachyandesite include clinopyroxene, phlogopite, olivine, and sanidine and the groundmass includes clinopyroxene, phlogopite, olivine, sanidine, apatite, Fe-Ti oxides, zircon, and glass. The phonotephlite-trachyandesitic dykes intruding the Pagu pluton mainly contain clinopyroxene (10%–20%), phlogopite (5%–10%), hornblende (20%–25%), sanidine (35%–45%), orthopyroxene (<3%), and olivine (<3%), with accessory minerals of zircon, apatite, and Fe-Ti oxides. Based on the variable clinopyroxene (Cpx) textures, they can be divided into two types: (1) type I Cpx commonly form crystal aggregations and show pervasive resorption textures (Figs. 3A, 3B, 3E, and 3G); (2) type II Cpx are commonly euhedral crystals and show zoning textures sometimes (Figs. 3C, 3F, and 3H–3K). The calc-alkaline intrusions collected from the WHS and EHS are fine-grained (0.5–2 mm) two-mica granites (Figs. 3L–3N). They are mainly composed of quartz (25%–35%), plagioclase (25%–40%), K-feldspar (15%–35%), biotite (1%–15%), and muscovite (1%–8%), with accessory minerals of zircon, titanite, epidote, garnet, apatite, and Ti-Fe oxides.

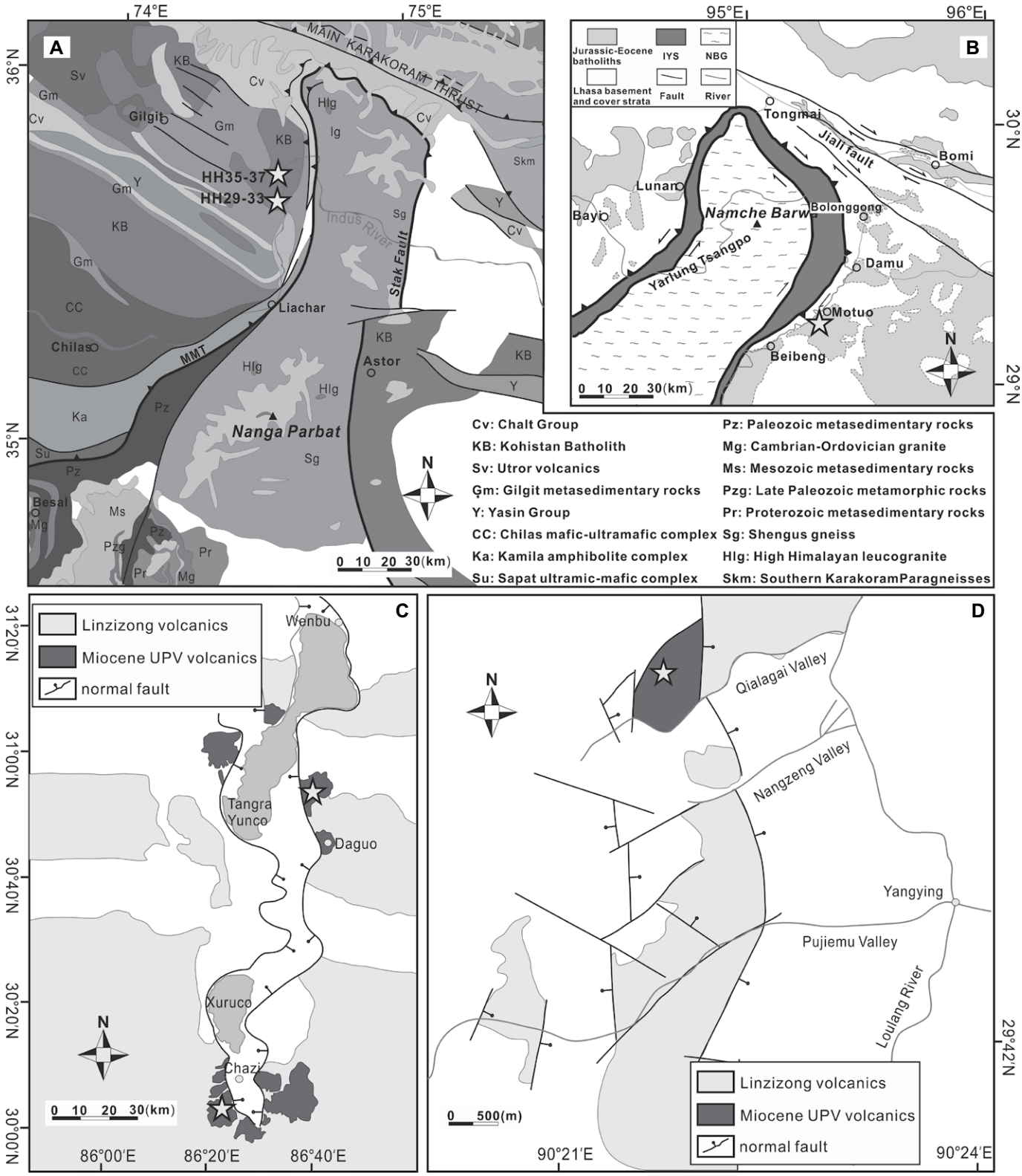

Figure 2. (A) Tectonic map of the Western Himalayas Syntaxes shows sample locations of two-mica granite (see Fig. 1A for locations). MMT—Main Mantle Thrust; KB—Kohistan Batholith; NP—Nanga Parbat, modified after 1:650,000 regional geological map. (B) Tectonic map of Eastern Himalayan Syntaxes shows Indus/Yarlung Tsangpo Suture zone (IYS) and Namche Barwa, modified after Pan et al. (2012). (C) Simplified tectonic map shows distribution of post-collisional ultrapotassic-potassic volcanic rocks in the N-S–trending TangraYumco-Xuruco rift, modified from Guo et al. (2013). (D) Simplified tectonic map of the Yangying post-collisional potassic volcanic rocks, modified from Zhang et al. (2017b).

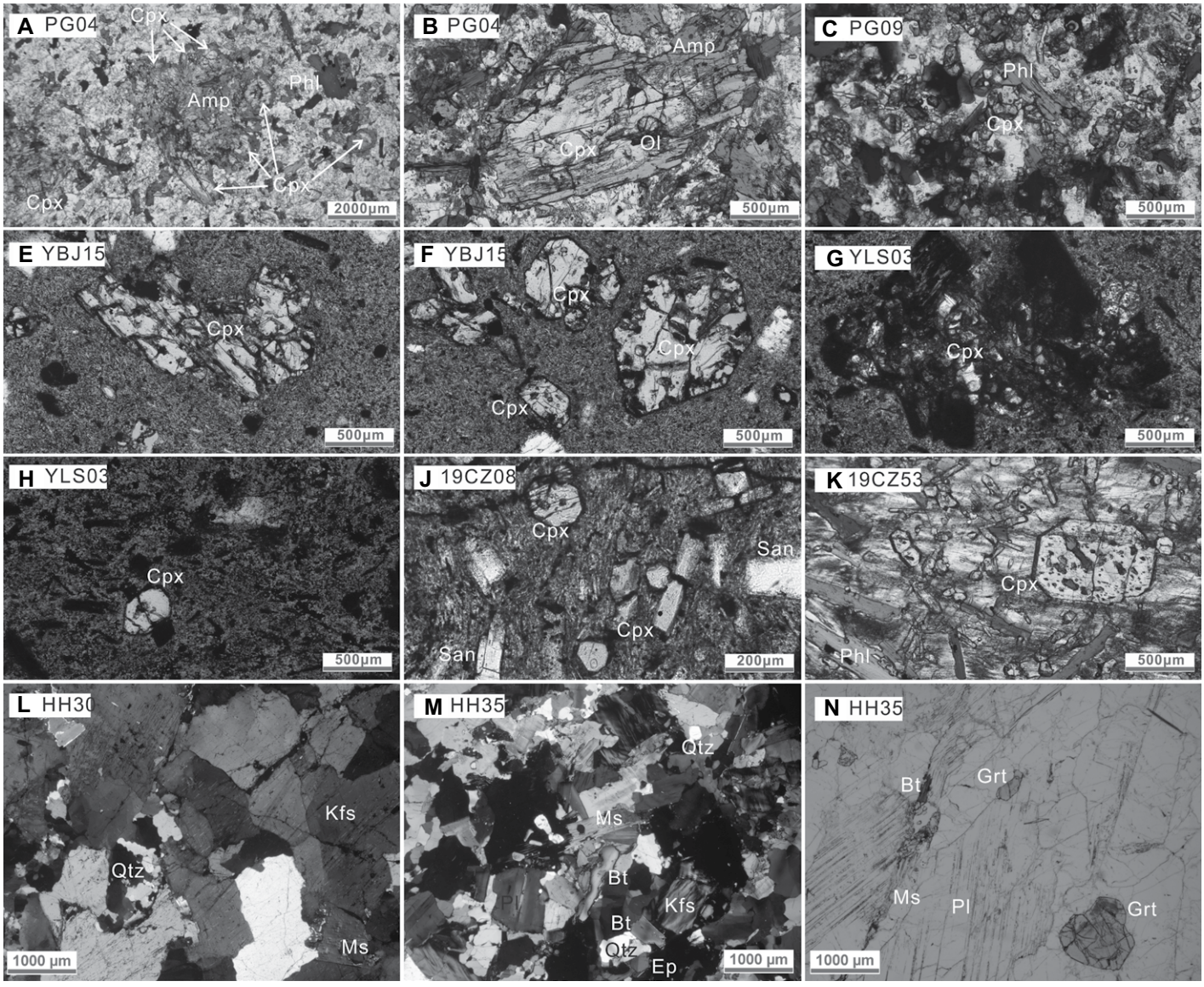

Figure 3. (A–K) Microphotographs of the Miocene ultrapotassic-potassic volcanics from the central Lhasa terrane of southern Tibet. (L–N) Microphotographs of the Oligocene two-mica granite from the Kohistan Island arc of southern Tibet. Bi—biotite; Hb—hornblende; Cpx—clinopyroxene; Opx—orthopyroxene; Pl—plagioclase; Qtz—quartz; Kfs—K-feldspar; San—sanidine; Ms—muscovite; Tit—titanite; Ep—epidote; Grt—garnet.

ANALYTICAL METHODS

Whole-rock samples were analyzed for major elements, using a Shimadzu sequential X-ray fluorescence spectrometer (XRF-1800) at the State Key Laboratory of Geological Processes and Mineral Resources (GPMR), China University of Geosciences, Wuhan, China. Loss on ignition (LOI) was determined by weight loss after drying at 1000 °C. The results obtained from Chinese national standards and repeated samples show analytical uncertainties of the XRF data of ~1% for element contents >10 wt% and ~5% for element contents <1.0 wt%. More details about the analytical procedures were described in Ma et al. (2012). The analytical uncertainty is generally <5%. Trace elements, including rare earth element (REE), were measured using Agilent 7500a inductively coupled plasma–mass spectrometry (ICP-MS) at GPMR. Zhang et al. (2017a) showed detailed sample-digesting procedure for ICP-MS analysis and analytical precision and accuracy.

Major element compositions of minerals were determined at GPMR, with a JEOL JXA-8230 electron probe microanalyzer (EPMA) equipped with five wavelength-dispersive spectrometers. The samples were first coated with a thin conductive carbon film prior to analysis. During the analysis, an accelerating voltage of 15 kV, a beam current of 10 nA, and a 2–5 μm spot size were used to analyze minerals. Data were corrected online using a ZAF (atomic number, absorption, fluorescence) correction procedure. The peak counting time was 10 s for Na, Mg, Al, Si, K, Ca, Fe, P, Cr and 20 s for Mn, Ti. The background counting time was one-half of the peak counting time on the high- and low-energy background positions. The following standards were used: jadeite (Na), olivine (Si), pyrope garnet (Al), diopside (Ca, Mg), sanidine (K), rutile (Ti), almandine garnet (Fe), rhodonite (Mn), apatite (P), chromium oxide (Cr).

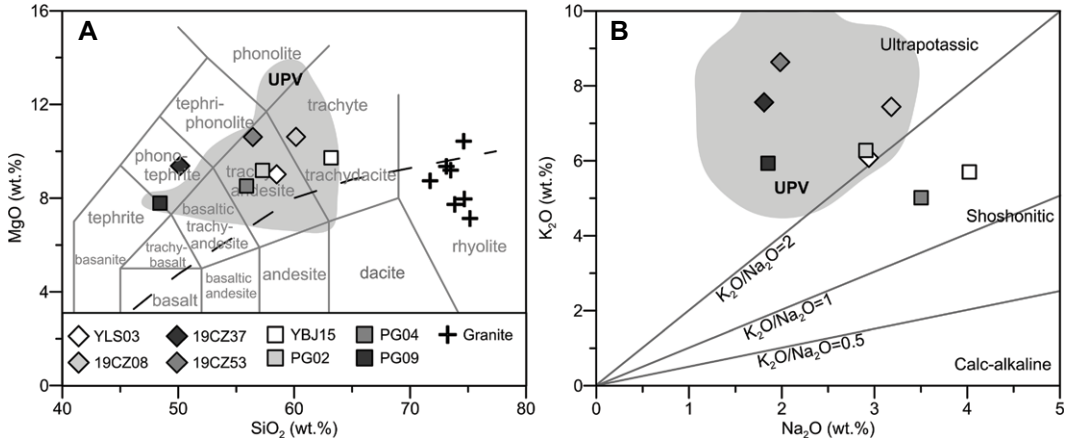

Figure 4. (A) $Na_2O + K_2O$ versus SiO_2 and (B) K_2O versus Na_2O diagrams for the two-mica granites from the west Himalayan syntaxis and the east Himalayan syntaxis and the ultrapotassic-potassic volcanics from the central Lhasa terrane of southern Tibet. UPV—ultrapotassic-potassic volcanic rocks.

U-Pb zircon dating was conducted by laser ablation ICP-MS at GPMR. Zircon 91500 was used as the external standard for U-Pb dating, and was repeatedly analyzed every five analyses. Time-dependent drifts of U-Th-Pb isotopic ratios were corrected using a linear interpolation (with time) for every five analyses according to the variations of zircon 91500 (i.e., two zircon 91500 + five samples + two zircon 91500) (Liu et al., 2010). Preferred U-Th-Pb isotopic ratios used for zircon 91500 are from Wiedenbeck et al. (Wiedenbeck et al., 1995). The uncertainties of preferred values for the external standard zircon 91500 were propagated to the combined errors of the samples. Concordia diagrams and weighted mean calculations were made using Isoplot/Ex_ver3 (Ludwig, 2003). Trace elements of the external standard zircon 91500 are present in Supplemental Data S2, and their mean values are roughly comparable with the published data (Liu et al., 2010).

RESULTS

Major and Trace Elements

The calc-alkaline intrusions from the WHS and EHS are weakly peraluminous (A/CNK = 1.00–1.08) and contain high SiO_2 (71.72–75.16 wt%) and Al_2O_3 (14.03–15.28 wt%) and variable K_2O (1.95–7.72 wt%) with K_2O/Na_2O of 0.4–2.9. They are relatively enriched in Rb, Ba, Th, and U and show strongly variable total REE contents (5.2–110.6 ppm) and fractionated REE patterns [$(La/Yb)_N$ = 3–65].

The ultrapotassic-potassic rocks have a wide range of SiO_2 contents (48.4–63.2 wt%), and high MgO (>3 wt%, except sample YBJ15) and K_2O (5.0–8.6 wt%) contents with high K_2O/Na_2O ratios of 1.4–4.4 (Fig. 4). They contain low TiO_2 (0.75–1.47 wt%) and CaO (3.19–7.86 wt%) contents and high Cr (423–48 ppm) and Ni (284–24 ppm) contents. They showed comparable enrichment of Rb, Ba, Th, and light-REE values and negative high field strength element (e.g., Nb, Ta, P, and Ti) anomalies in the trace element spider diagram (Fig. 5A). In the chondrite-normalized REE pattern, these mafic

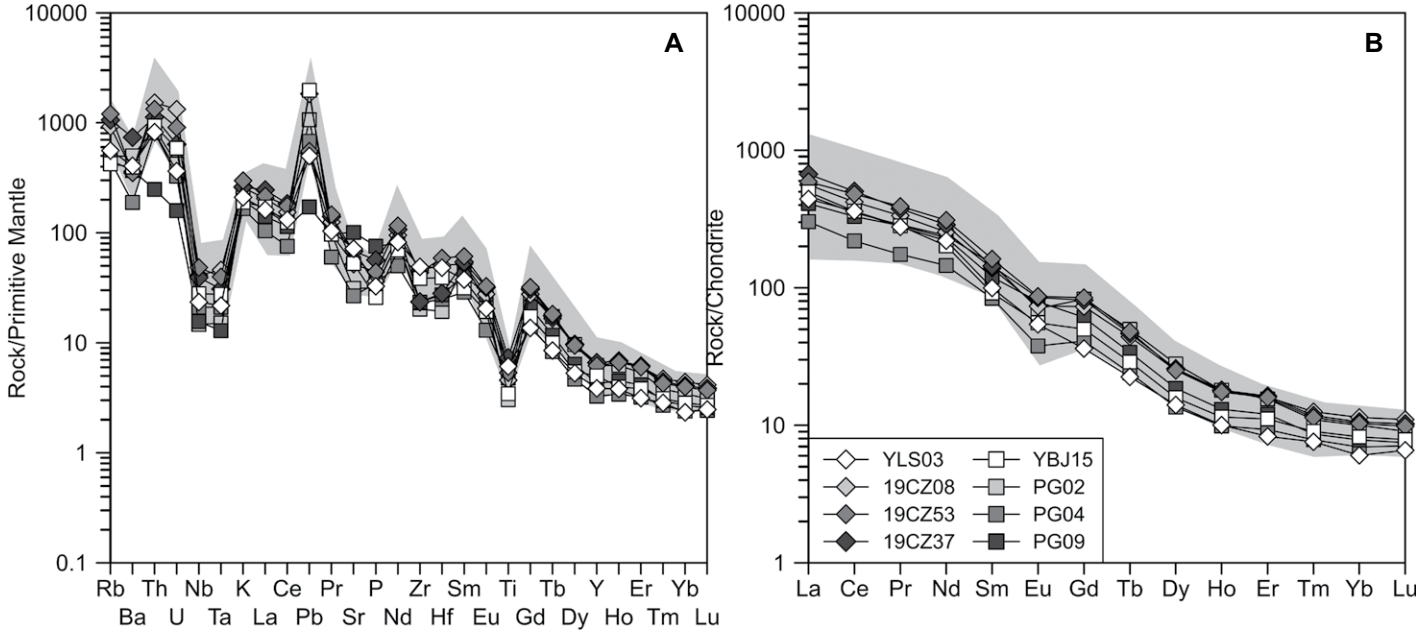

Figure 5. (A) Primitive mantle-normalized element spider diagrams and (B) Chondrite-normalized rare earth element patterns for the ultrapotassic-potassic volcanics from the central Lhasa terrane of southern Tibet. Normalizing values are from Sun and McDonough (1989).

intrusions displayed fractionated REE patterns with $(La/Yb)_N$ ratios of 44–73 and no obvious Eu anomalies (Eu/Eu* = 0.63–0.93) (Supplemental Data S1; Fig. 5B).

U-Pb Zircon Geochronology

Zircons from the studied two-mica granites in the WHS and EHS are commonly euhedral, with variable crystal lengths of 50–400 μm and aspect ratios of 1:1–6:1 (Fig. 6). In CL images, they commonly show dark color and clear oscillatory zoning or patchy zoning (Fig. 6). A few zircons showing light color could be inherited or captured zircons (Figs. 6C and 6E). Zircons from the potassic-ultrapotassic rocks are euhedral to subhedral, with crystal lengths of 50–100 μm and aspect ratios of 1:1–3:1. Two types of zircons are recognized based on CL imaging (Figs. 6J–6Q). Zircons in samples YLS03, PG09, and YBJ15 show clear broad oscillatory zoning and sector zoning, while zircons in the other four samples show clear oscillatory zoning. The U-Pb zircon age data are given in Table S1.

Twelve analyses from sample HH-29 yield $^{206}Pb/^{238}U$ ages between 32.0 ± 0.5 Ma and 34.3 ± 0.7 Ma, with a weighted mean of 32.7 ± 0.5 Ma (mean square weighted deviation [MSWD] = 3.0) (Fig. 7A). Thirteen analyses from sample HH-30 yield $^{206}Pb/^{238}U$ ages between 21.8 ± 0.3 Ma and 22.9 ± 0.2 Ma, with a weighted mean of 22.4 ± 0.2 Ma (MSWD = 2.3) (Fig. 7B). Eleven analyses from sample HH-31 give $^{206}Pb/^{238}U$ ages ranging from 29.5 ± 0.6 Ma to 32.7 ± 0.8 Ma, with a weighted mean of 31.6 ± 0.5 Ma (MSWD = 4.0) (Fig. 7C). Fifteen analyses from sample HH-33 yield $^{206}Pb/^{238}U$ ages between 30.1 ± 0.3 Ma and 32.1 ± 0.6 Ma, with a weighted mean of 31.0 ± 0.4 Ma (MSWD = 3.6) (Fig. 7D). For sample HH-35, seven U-Pb isotopic analyses on zircon crystals give $^{206}Pb/^{238}U$ ages varying from 21.4 ± 0.3 Ma to 22.0 ± 0.3 Ma, with a weighted mean of 21.5 ± 0.2 Ma (MSWD = 0.7) (Fig. 7E). Fourteen analyses from sample HH-36 yield $^{206}Pb/^{238}U$ ages between 29.9 ± 0.6 Ma and 33.5 ± 0.7 Ma, with a weighted mean of 32.0 ± 0.6 Ma (MSWD = 4.8) (Fig. 7F). Twelve analyses from sample HH-37 yield $^{206}Pb/^{238}U$ ages ranging from 27.4 ± 0.2 Ma to 29.3 ± 0.3 Ma, with a weighted mean of 28.2 ± 0.4 Ma (MSWD = 4.4) (Fig. 7G). Twelve analyses from sample T974 yield $^{206}Pb/^{238}U$ ages ranging from 29.0 ± 0.5 Ma to 30.5 ± 0.8 Ma, with a weighted mean of 29.7 ± 0.4 Ma (MSWD = 4.4) (Fig. 7H).

Twelve analyses from sample YLS03 yield $^{206}Pb/^{238}U$ ages between 12.7 ± 0.5 Ma and 14.3 ± 0.6 Ma, with a weighted mean of 13.8 ± 0.2 Ma (MSWD = 0.9) (Fig. 7J). Eleven analyses from sample 19CZ08 yield $^{206}Pb/^{238}U$ ages between 10.9 ± 0.2 Ma and 11.8 ± 0.3 Ma, with a weighted mean of 11.2 ± 0.2 Ma (MSWD = 1.1) (Fig. 7K). Twelve analyses from sample 19CZ37 give $^{206}Pb/^{238}U$ ages ranging from 10.9 ± 0.63 Ma to 11.7 ± 0.3 Ma, with a weighted mean of 11.3 ± 0.1 Ma (MSWD = 1.1) (Fig. 7L). Eleven analyses from sample 19CZ53 yield $^{206}Pb/^{238}U$ ages between 11.0 ± 0.2 Ma and 12.1 ± 0.3 Ma, with a weighted mean of 11.4 ± 0.1 Ma (MSWD = 1.0) (Fig. 7M). For sample YBJ15, twelve U-Pb isotopic analyses on zircon crystals give $^{206}Pb/^{238}U$ age intercepted at 10.2 ± 0.6 Ma (MSWD = 2.1) (Fig. 7N). Twelve analyses from sample PG02 yield $^{206}Pb/^{238}U$ ages between 14.0 ± 0.4 Ma and 15.8 ± 0.4 Ma, with a weighted mean of 15.0 ± 0.4 Ma (MSWD = 2.6) (Fig. 7O). Twelve analyses from sample PG04 yield $^{206}Pb/^{238}U$ ages ranging from 14.1 ± 0.4 Ma to 15.4 ± 0.4 Ma, with a weighted mean of 14.6 ± 0.3 Ma (MSWD = 1.8) (Fig. 7P). Ten analyses from sample PG09 yield $^{206}Pb/^{238}U$ age intercepted at 10.7 ± 0.4 Ma (MSWD = 3.0) (Fig. 7Q).

Mineral Composition

Clinopyroxenes in the ultrapotassic-potassic rocks from both Chazi (86°E) and Pagu-Yangying (90°E) are composed of diopside and augite. They have high MgO and FeO contents with Mg# of 92–63 (Table S2; Fig. 8). The augite

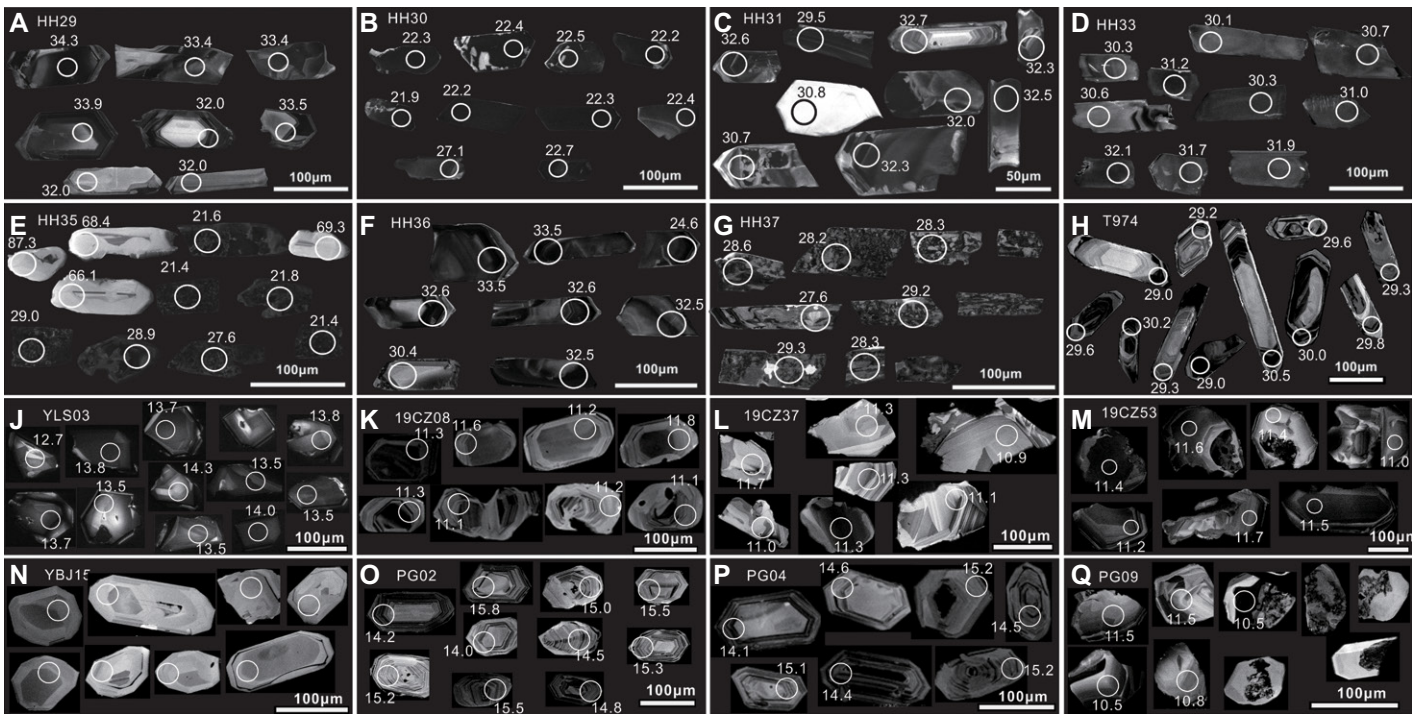

Figure 6. Representative cathodoluminescence images for zircons from the granitoid samples (A) HH29, (B) HH30, (C) HH31, (D) HH33, (E) HH35, (F) HH36, (G) HH37, and (H) T974 from the west Himalayan syntaxis and the east Himalayan syntaxis of southern Tibets, and the ultrapotassic-potassic samples (J) YLS03, (K) 19CZ08, (L) 19CZ37, (M) 19CZ53, (N) YBJ15, (O) PG02, (P) PG04, and (Q) PG09.

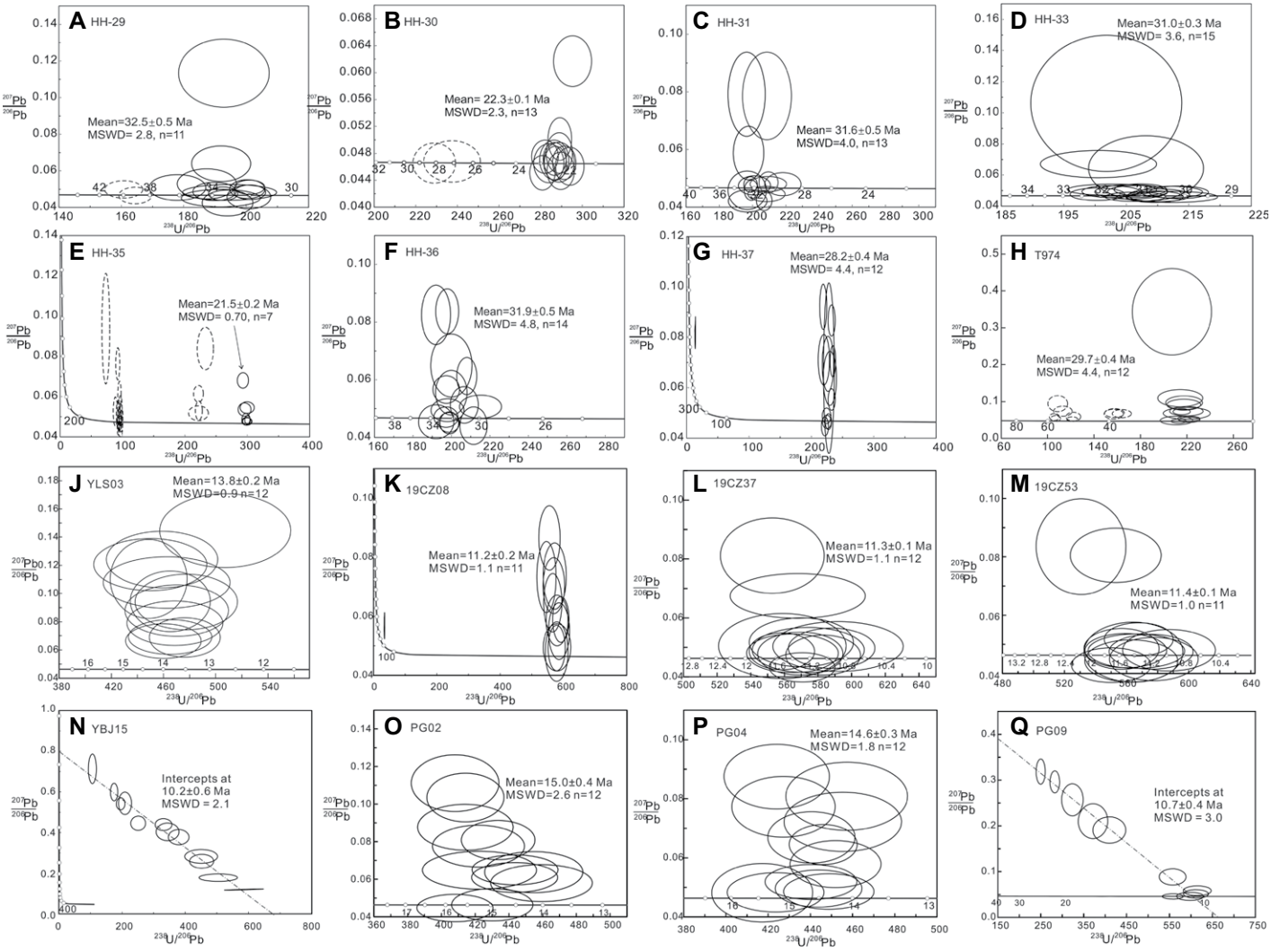

Figure 7. U-Pb Tera-Wasserburg plots for U-Pb zircon analyses from the granitoid samples (A) HH29, (B) HH30, (C) HH31, (D) HH33, (E) HH35, (F) HH36, (G) HH37, and (H) T974 from the west Himalayan syntaxis and the east Himalayan syntaxis of southern Tibet and the ultrapotassic-potassic samples (J) YLS03, (K) 19CZ08, (L) 19CZ37, (M) 19CZ53, (N) YBJ15, (O) PG02, (P) PG04, and (Q) PG09. MSWD—mean square weighted deviation.

grains have higher Al_2O_3 and TiO_2 contents, and similar Na_2O, compared to those of the diopside grains for both the Chazi (86°E) and Pagu-Yangying (90°E) ultrapotassic-potassic rocks. A few augite grains from sample PG04 contain slightly higher Cr_2O_3 contents than other clinopyroxene grains. The variable Mg# values of clinopyroxene in these samples indicate that they have experienced magmatic evolution with varying degrees.

The temperature and pressure conditions of these evolved magmas are estimated from multiple geobarometers and thermometers (Ferry and Watson, 2007; Neave and Putirka, 2017; Putirka, 2008), which are listed in Table S2 and Supplemental Data S2. The estimated Cpx temperature data are tested for equilibrium conditions using three criteria: (1) the estimated Fe-Mg exchange coefficient is 0.27 ± 0.03 (Table S2); (2) the predicted and observed Cpx components are roughly comparable (Table S2); (3) estimated results from multiple Cpx thermometers are also comparable (Fig. 8). $T_{P2008\text{-}33}$, $T_{P2008\text{-}34}$, and $T_{P2008\text{-}32d}$ thermometers show that most of the clinopyroxene grains formed under temperatures ranging from 1150 to 900 °C (Table S2; Fig. 8).

The substitution of Ti in zircon is primarily for Si (Ferry and Watson, 2007). Thus, the Ti-in-zircon thermometer depends on the activity of SiO_2 (a_{SiO2}) and TiO_2 (a_{TiO2}). According to their SiO_2 and TiO_2 contents, a_{SiO2} and a_{TiO2} are 1 and 0.7 for the granitoids from the WHS and EHS and 0.7 and 0.9 for the ultrapotassic-potassic rocks (except sample YBJ15), respectively. a_{SiO2} and a_{TiO2} are 0.9 and 0.7 for sample YBJ15 for its relatively higher SiO_2 and lower TiO_2 contents (Supplemental Data S2). Ti-in-zircon thermometry indicates that most magmatic zircons from the WHS and EHS crystallized in the range 600–750 °C (Supplemental Data S2), while zircons from the central Lhasa terrane (85°E to 90°E) show higher crystallization temperatures (700–900 °C; see Supplemental Data S2). These estimated temperatures are coincident with the formation of the WHS and EHS zircons and the central Lhasa terrane zircons in silicic magmas and mafic-intermediate magmas, respectively.

DISCUSSION

Spatiotemporal Variations of Post-Collisional Magmatism in Southern Tibet

The U-Pb zircon age data show that the magma crystallization ages of the two-mica

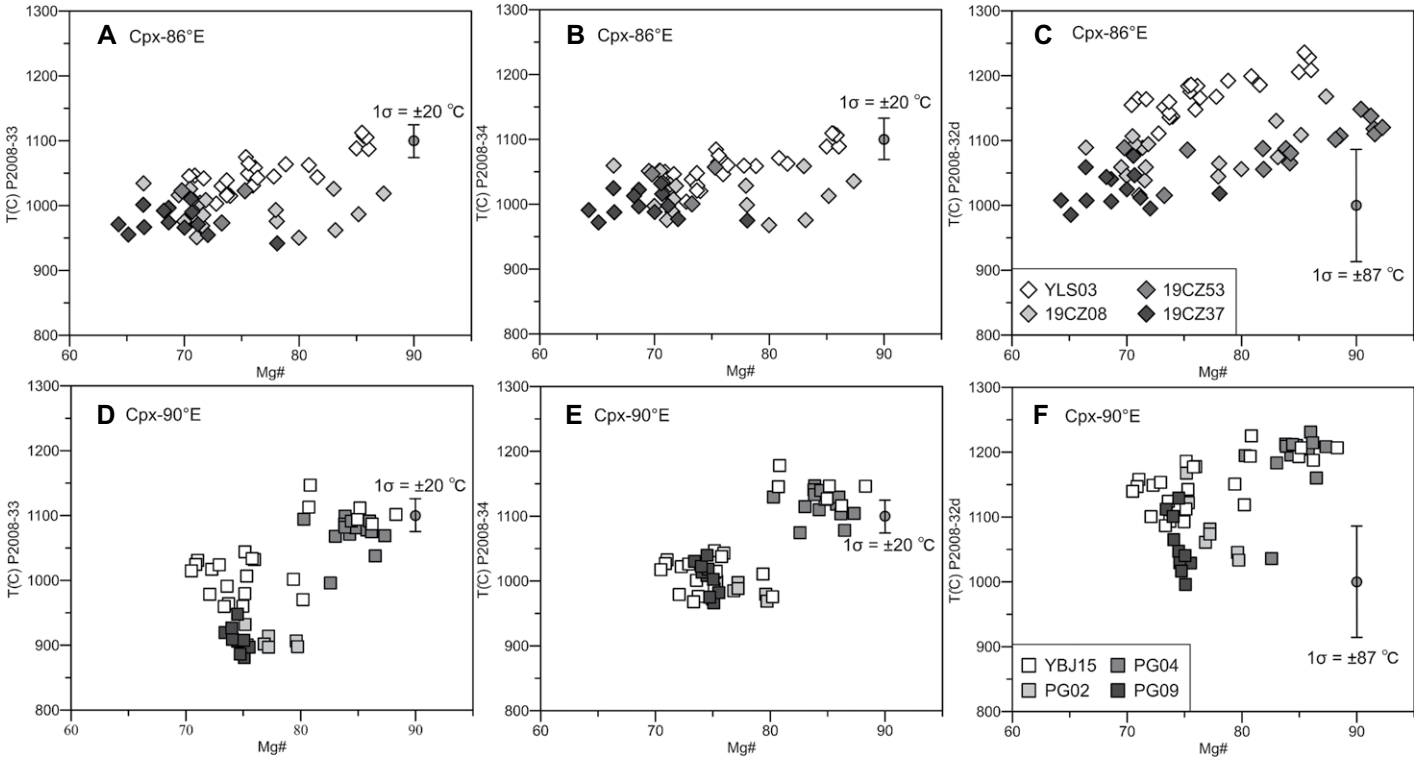

Figure 8. (A, B, D, and E) Jd-DiHd exchange thermometer, (C) and (F) revised clinopyroxene-only thermometer for the Miocene ultrapotassic-potassic volcanics from 86°E and 90°E in the central Lhasa terrane of southern Tibet. Cpx—clinopyroxene.

granite and ultrapotassic-potassic rocks in this study lie in the ranges of 33–22 Ma and 15–10 Ma (Supplemental Data S1), respectively. In order to depict an integrated spatial-temporal evolution of the post-collisional magmatism in southern Tibet, we summarize 107 samples from the Oligocene–Miocene potassic-ultrapotassic rocks and 105 samples from coeval calc-alkaline magmatic rocks published in this region (Table S3; Fig. 1B). Our age data, together with the age data in the literature, show roughly three decreasing age variations from 75°E to 90°E (from 33 to 19 Ma for 74°E–79°E, from 26 to 15 Ma for 80°E–85°E, and from 23 to 18 Ma for 85°E–90°E) and one decreasing age variation from 30 to 20 Ma for 95°E–90°E (Fig. 1B).

Our former geochronological results of the post-collisional calc-alkaline rocks in the east Himalayan syntaxis formed between 30 and 21 Ma and exhibited a decreasing age variation from east to west in the eastern part of the Lhasa terrane (Pan et al., 2012). The two-mica granite samples in the west Himalayan syntaxis exhibit comparable formation ages (33–22 Ma). Some existing Oligocene outliers do not follow the decreasing trends described above. These intrusions are characterized by small volumes and 5–15 m.y. earlier than the dominant magmatism flares along the neighboring longitude, which might be locally formed by the hysteretic response to the break-off of the Neo-Tethyan oceanic slab.

Melting Depth Variations of the Ultrapotassic-Potassic Rocks

The ultrapotassic rocks in southern Tibet are considered to be primarily derived from a metasomatized mantle source and then contaminated by ancient crustal materials (Guo et al., 2015; Miller et al., 1999; Williams et al., 2004; Zhao et al., 2009). All the analyzed ultrapotassic-potassic rocks—except sample YBJ15—have high MgO (3.16–9.18 wt%) and K_2O (5.01–8.63 wt%) contents with K_2O/Na_2O ratios of 1.43–4.35, and high Cr (76.5–423 ppm) and Ni (57.1–284 ppm) (Supplemental Data S1). They show comparable geochemical compositions with these ultrapotassic magmas (Figs. 4 and 5). These features imply that these rocks are mantle-derived. Sample YBJ15 exhibits consistent trace-element composition patterns with other ultrapotassic-potassic rocks in this study (Fig. 5), suggesting that it is also mantle-derived.

Mantle-derived melts were commonly originated from partial melting of peridotite (Walter, 1998), which is the dominant component in the upper mantle (Green and Ringwood, 1967). However, silica-deficient alkali melts, generally containing higher SiO_2 and Ni contents and lower MgO and CaO contents than those of peridotite-derived melts (Herzberg, 2011), were increasingly attributed to partial melting of the pyroxenite source (Dasgupta et al., 2010; Lambart et al., 2013). The ultrapotassic magmas in southern Tibet show high SiO_2 and Ni concentrations and relatively low MgO and CaO contents, which indicate derivation from partial melting of the pyroxenitic mantle source (Guo et al., 2015). Our samples show comparable geochemical compositions with these ultrapotassic magmas (Figs. 4 and 5), implying that they were also originated from the pyroxenite source.

The melting pressure of pyroxenite-derived primary melts can be constrained by the reverse model (Herzberg, 2011). High-Mg (>7 wt%) ultrapotassic rocks are relatively rare, and nearly 100 samples have been published in the study area. Energy-constrained assimilation and fractional crystallization modeling showed that crustal assimilation would be limited (<7% for mafic magma with temperatures as high as 1300 °C) for such magmas during their emplacement (Dai et al., 2021). Thirteen ultrapotassic samples (including two samples in this study) are collected to calculate their melting depth (Table S4). These samples have MgO content of more than 8 wt% and LOI of less than 1.5 wt%, which exhibit whole-rock geochemical characteristics

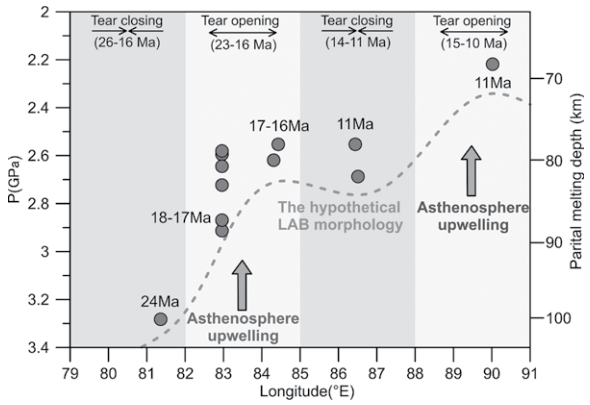

Figure 9. Melting pressure of the ultrapotassic rocks from Bongba (81°E) to Pagu (90°E) in southern Tibet. The primary melts are calculated by adding or subtracting olivine to lavas that experienced only olivine fractionation, and involves lavas with MgO >8% for the ultrapotassic rocks in southern Tibet. The iteration is stopped when the melt composition is coincident with the cotectic [L + Opx + Cpx + Gt] or [L + Ol + Cpx + Gt] as constrained by the pressure P(GPa) = exp[1.6748 −0.0838(A-0.5389CS)], CS = CaO + 2(Na_2O + K_2O) −3·333P_2O_5, A = TiO_2 + Al_2O_3 + Cr_2O_3 + Na_2O + K_2O (Herzberg, 2011). We described "the hypothetical LAB morphology" here to discuss the variable morphology of the lithosphere-asthenosphere boundary rather than its true depth. L—melt; Opx—orthopyroxene; Cpx—clinopyroxene; Gt—garnet.

dominated by fractionation of olivine with insignificant crustal assimilation. For assumptions of depth calculations, see the caption of Figure 9. The estimated pressures, ranging from 3.28 to 2.22 GPa, show that the melting depth is progressively decreasing from west (100 km in Bongba) to east (70 km in Pagu), and two melting pressure undulations (18–16 Ma for the Sailipu and Zabuye samples and 11 Ma for the Pagu sample) are present in the low-velocity zones (Fig. 9).

Temperature Variations of the Ultrapotassic-Potassic Rocks

As the studied ultrapotassic-potassic rocks were originally derived from the metasomatized mantle, mantle melting temperature variations could probably be recorded by some minerals which crystallized during magma ascent. Temperatures calculated using a Cpx Jd-DiHd exchange thermometer show decreasing variations associated with decreasing Cpx Mg# values (Figs. 10A and 10B), indicating crystallization during different stages of magma differentiation. For the ultrapotassic rocks along 86°E (Figs. 10A and 10C), Cpx temperatures of the older (14 Ma) sample YLS03 range from 1019 to 1110 °C, and show systematically higher values (ΔT = 50 °C) than those of the younger (11 Ma) samples (954–1039 °C). In contrast, the ultrapotassic-potassic rocks along 90°E show opposite Cpx temperature variations (Fig. 10B) in that the younger samples (YBJ15 and PG09 of 10 Ma) have higher crystallization temperatures than the older samples (PG02 and PG04 of 15 Ma) (Figs. 10A and 10B). Together with the crystal texture features and estimated pressure results (Fig. 10D; Table S1), the type I Cpx from samples PG04 and YBJ15 have higher Mg# (80–88) and crystallization temperatures (1050–1100 °C for PG04 and 1100–1150 °C for sample YBJ15), which could reflect the initial magma temperature in the lower crust and show 50 °C increases from 15 to 10 Ma. Both these two magma pulses show 150–200 °C decreases recorded by type II Cpx (Fig. 10D), which might indicate retention in the lower crust. Decreasing clinopyroxene

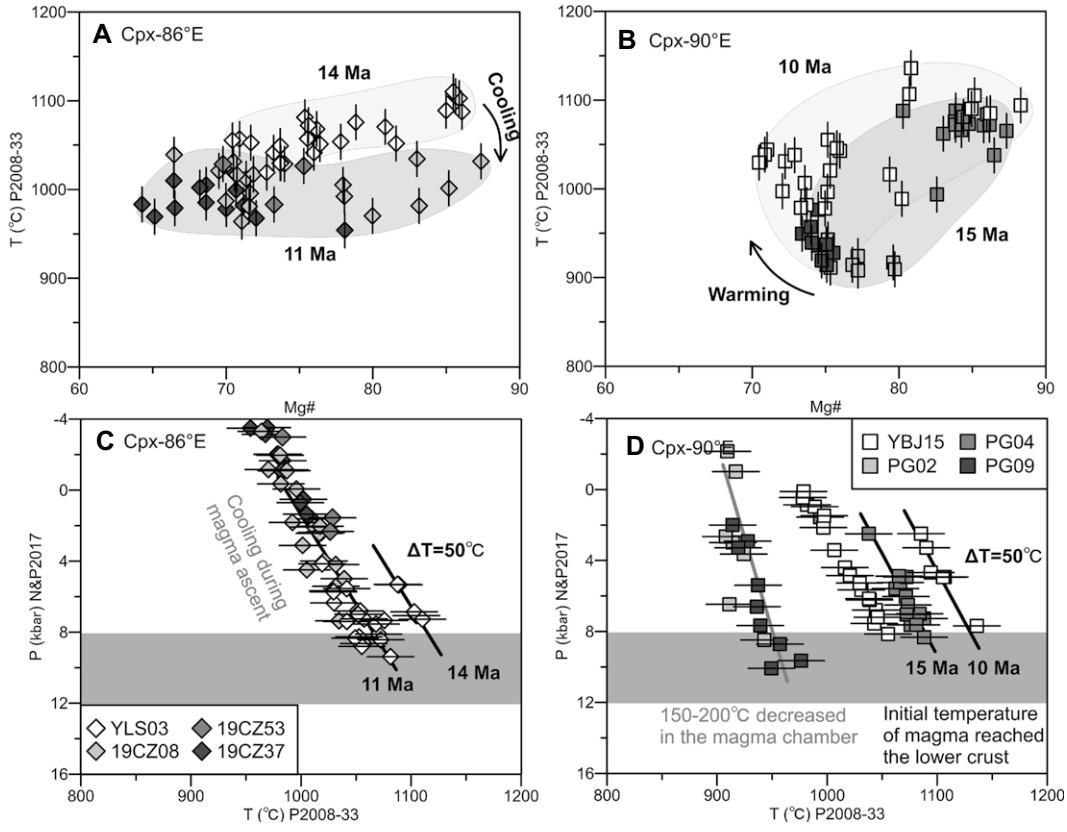

Figure 10. (A and B) Liquidus temperatures of clinopyroxene; (C and D) pressure (P) versus temperature (T) plots for the Miocene ultrapotassic-potassic volcanics from 86°E and 90°E in the central Lhasa terrane. P and T are calculated according to the geothermometer in Neave and Putirka (2017). Cpx—clinopyroxene; T—temperature; P—pressure.

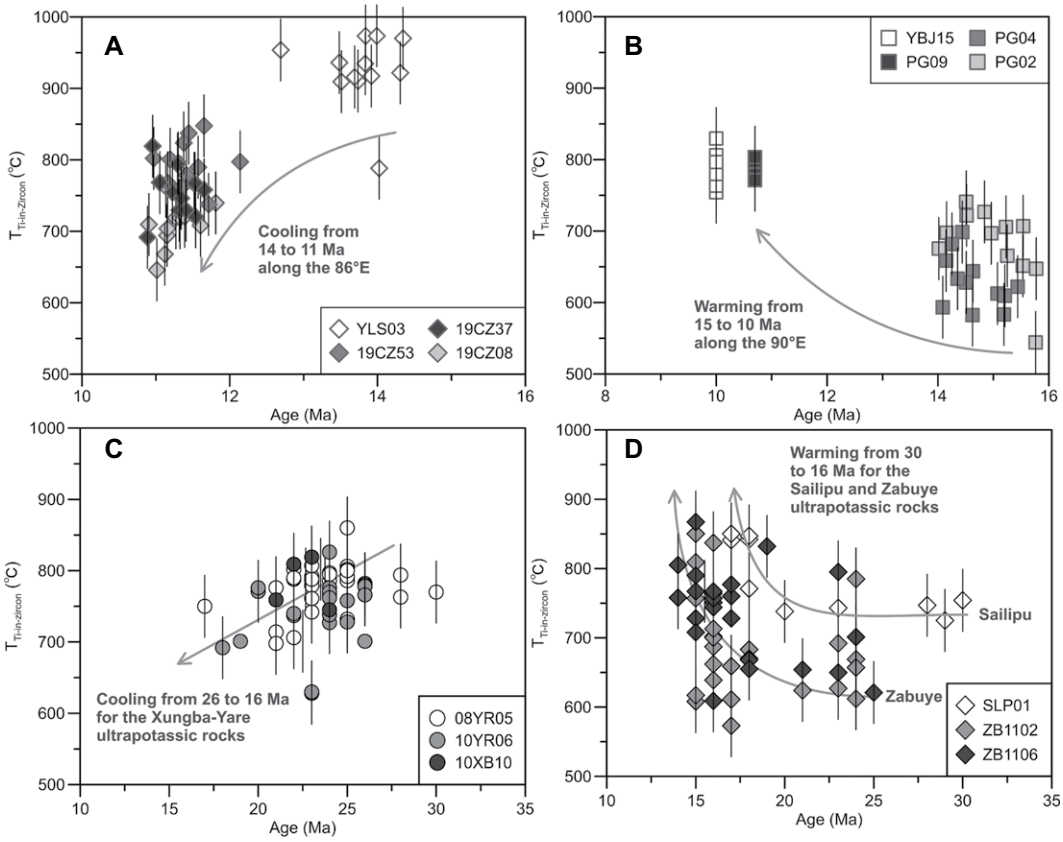

Figure 11. Ti-in-zircon temperature variations for zircons from the Miocene ultrapotassic-potassic volcanic rocks in the central Lhasa terrane of southern Tibet. (A) For samples from 86°E and 90°E, (B) for samples from Xungba and Yare, (C) for samples from Sailipu, and (D) for samples from Zabuye. Zircon trace elements data for the samples from Xungba, Yare, Sailipu, and Zabuye are from Liu et al. (2014). T—temperature.

crystallization temperatures are consistent with their crystallization depths decreasing from pressures of 12–8 kbar to 4–0 kbar during magma ascent (Figs. 10C and 10D).

Zircon grains were present in the crystallization phases later than clinopyroxene in these ultrapotassic-potassic samples. Hence, they could record the late-stage magma temperature of these ultrapotassic-potassic rocks. Ti-in-zircon thermometry results for the ultrapotassic rocks from 86°E (Fig. 11A) also show that the older sample YLS03 has higher $T_{Ti\text{-}in\text{-}zircon}$ values (mostly >900 °C) compared to the younger samples ($T_{Ti\text{-}in\text{-}zircon}$ values = 670–830 °C). In contrast, the older ultrapotassic-potassic samples (PG02 and PG04) from 90°E (Fig. 11B) have relatively lower $T_{Ti\text{-}in\text{-}zircon}$ values (less than 700 °C), while the younger samples (PG09 and YBJ15) have higher $T_{Ti\text{-}in\text{-}zircon}$ values (more than 770 °C).

In summary, the multiple thermometry, based on clinopyroxene and zircon which represent the progressive crystallization phases during magma ascent, exhibit a temporal decrease in magma temperatures from 14 to 11 Ma along a longitude of 86°E and an increasing temperature trend from 15 to 10 Ma along longitude 90°E in the central part of the Lhasa terrane. Therefore, such temperature/time trends are likely to record regional temperature variations (ΔT = 50 °C) in the deeper mantle source and are spatially consistent with the high-velocity zone (86°E) and the low-velocity zone (90°E) at depth of 135 km, respectively (Fig. 1).

Interestingly, the opposing magma temperature variations (Figs. 11C and 11D) were also recorded by the Oligocene–Miocene zircons in the Xungba-Sailipu ultrapotassic rocks from the western domain of the Lhasa terrane (Liu et al., 2014). Mantle seismic tomography images (depth at 135 km) in this area show that low-velocity and high-velocity zones are present under the Xungba-Yare area and the Sailipu and Zabuye area (Fig. 1A), respectively. Published data exhibit a decreasing $T_{Ti\text{-}in\text{-}zircon}$ trend for the Oligocene–Miocene magmatic zircons from the Xungba-Yare ultrapotassic rocks and an increasing $T_{Ti\text{-}in\text{-}zircon}$ trend for the Oligocene–Miocene magmatic zircons from the Sailipu and Zabuye ultrapotassic rocks. These features suggest that the zircon crystallization temperatures of these rocks and the mantle lithospheric morphology are also coupled.

Interplay between Continental Slab Tearing and Asthenospheric Flow

Late to post-collisional magmatism in orogens has many causes (Kusky and Wang, 2022), including slab break-off (failure) or tear-related plutonism (Davies and von Blanckenburg, 1995; Dilek and Sandvol, 2009), crustal thickening, orogenic collapse (Dewey, 1988; Kusky, 1993), and core-complex formation (Whitney et al., 2013), or large-scale lithospheric foundering (Bird, 1978; Zheng et al., 2022). Magmatism from these various sources differ from earlier arc-related magmas, in that they tend to be distributed for up to hundreds of km from associated sutures and can last for tens of millions of years after the main collision (Kusky and Wang, 2022). Slab break-off and tear-related magmatism are typically characterized by higher Th values than those from the normal mantle array due to involvement of earlier subducted sediments (particularly if passive margins are subducted), and tend to develop increasingly alkaline geochemical characteristics with time, due to increasing asthenospheric input with time (Wilson and Bianchini, 1999; Hildebrand et al., 2018; Kusky and Wang, 2022). In addition, plutons of these suites intrude late during the collision-related deformation so they cross-cut earlier structures, but typically experience additional later flattening, deforming the plutons into domal structures (e.g., Hildebrand et al., 2018; Kusky et al., 2021; Kusky and Wang, 2022).

The Neogene magmatism and E-W extensional faulting in the Tibetan Plateau have been attributed to the convective removal of

the Tibetan sub-continental lithospheric mantle (Chen et al., 2017; Chung et al., 2003; Coleman and Hodges, 1995; Turner et al., 1993; Williams et al., 2004; Wu et al., 2022). In contrast, movement of the N-S–trending normal faults and grabens is traced back to the early Miocene (23–14 Ma) and shows eastward propagation in southern Tibet (Bian et al., 2020; Coleman and Hodges, 1995; Mitsuishi et al., 2012; Blisniuk et al., 2001; Williams et al., 2001). Their ages are significantly younger (>10 m.y.) than the onset of post-collisional magmatism. Post-collisional mantle-derived mafic rocks are widely distributed in northern Tibet (Guo and Wilson, 2019; Turner et al., 1996), in contrast to the relatively local distribution of mafic rocks in the central and western Lhasa terrane in southern Tibet (Zhao et al., 2009). They are almost entirely absent in the Himalayan terrane where crustal anatexis events are widespread from Eocene to Miocene (Zhang et al., 2004). Furthermore, the age variations of the Oligocene–Miocene magmatic rocks seem unsystematic in southern and northern Tibet (Ding et al., 2007; Guo and Wilson, 2019), which is also unreconciled with the pervasive N-S–trending normal faults. Therefore, sinking of the Tibetan sub-continental lithospheric mantle does not appear to fully explain either the post-collisional magmatism or E-W–trending extension.

The Indian lithosphere is generally accepted to have been subducted northwards beneath southern Tibet as indicated by mantle tomographic images (Kosarev et al., 1999; Tilmann et al., 2003). The lower Indian crust is likely to have undergone ~30% eclogitization before descending to the Tibetan upper mantle (Schulte-Pelkum et al., 2005). This partially eclogitized lower crust of the Indian slab would result in the break-off of the Indian lithosphere due to its increasing density (Mahéo et al., 2002; Shi et al., 2020). The break-off model of the SIL is consistent with the scenario of a sudden decreasing convergence velocity (from ~85 mm/yr to 45 mm/yr) between the Indian and Asian blocks (van Hinsbergen et al., 2011), due to loss of the pull force associated with detachment of the partially eclogitized subducted slab.

Tearing of the SIL has been interpreted from mantle seismic tomography images (Chen et al., 2015; Li and Song, 2018; Liang et al., 2016; Liu et al., 2020), although the tearing positions and slab angles are debated. Li and Song (2018) reported high-resolution seismic tomography that shows four pieces of the torn SIL with different angles in southern Tibet. Slab windows along the sectors 82°E–85°E and 88°E–92°E in their tomography images show a strong relationship with the regional N-S–trending rifting (Fig. 1A), implying close links between the crustal deformation and the mantle lithosphere. Our collated age variations of the post-collisional magmatism in southern Tibet show some spatial consistency with the four sections of the torn SIL (Fig. 1). Diachronous break-off of the SIL is proposed to have resulted in the spatially decreasing variations of ages of the two-mica granites in the eastern portion of the Lhasa terrane (Pan et al., 2012; Zhang et al., 2014). Similarly, slab detachment was proposed to propagate eastward with the younging trend of the magmatic rocks in the western portion of the Lhasa terrane (Guo et al., 2015). Webb et al. (2017) summarized that slab tearing led to slab detachment initiating at both ends of the Himalaya at ca. 25 Ma, then migrated toward the central Himalaya. The compiled age results in this study further show that the post-collisional magmatism was initiated earlier in the EHS and WHS and had two age undulations in central southern Tibet (Fig. 1). Hence, we propose that four diachronous break-off events of the SIL occurred in southern Tibet during the Oligocene to Miocene.

Three-dimensional numerical models show that subducting continental lithosphere would be initially steep and then flex upwards and flattened below the overriding plate, after the break-off of the eclogitized slab at great depths (Magni et al., 2017). Diachronous break-off would lead to variable angles of the subducting continental lithosphere, which would be torn when the angle difference exceeds its limiting value in their models. It could lead to a contrasting evolution of the slab windows in southern Tibet: the 81°E (26–18 Ma) and 86°E (14–11 Ma) slab windows might be closed by the subsequent opening of the adjacent 85°E (25–15 Ma) and 90°E (15–10 Ma) slab windows, probably due to rebounding and lateral motion of the torn SIL impacted by the asynchronous asthenosphere upwellings (Fig. 12). These geodynamic processes could be the original causes for the

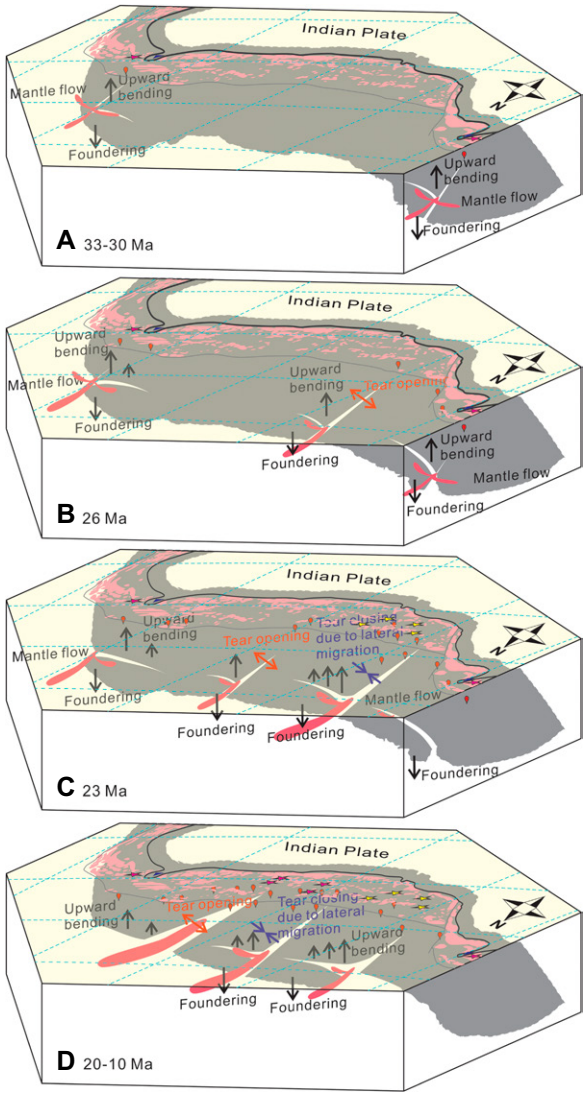

Figure 12. Schematic tectonic model for the evolution of the Oligocene–Miocene magmatism in southern Tibet corresponding to suture-perpendicular tearing and suture-parallel foundering of the subducted Indian plate. The pentagrams represent sample locations as in Figure 1. The gray regions depict the speculated pattern of the subducted Indian Plate from surface to depth of 135 km.

opposite variations of mantle-derived magma temperature observed in this study. The melting pressure variation probably indicates the progressive rising of the lithosphere-asthenosphere boundary (Figs. 1A and 9). The resultant asthenospheric upwelling distribution is consistent with the tearing of the SIL along 82°E–85°E and 88°E–92°E (Fig. 1A). Furthermore, lateral motion of the torn SIL caused local decoupling between the age spectrum of the post-collisional rocks and the recent mantle tomography (Fig. 1). For example, the mismatch along the 85–87°E sector, which might be one former slab window but is not clear from the tomography image, is probably a result of lateral motion of the torn SIL impacted by the asthenosphere upwelling along the 90°E after 15 Ma.

Ongoing diachronous break-off of the SIL has been reported in the Hindu Kush in Afghanistan based on seismic tomographic images (Kufner et al., 2021), which implies that it may be a common geodynamic process in a continental collision setting. In southern Tibet, magmatism associated with break-off of the SIL shows geochronological variations trending north-south. For example, magmatic records in the EHS show a south-to-north younging trend ranging from 29 to 21 Ma, while magmatism in the TangraYumco-Xuruco rift (86°E) shows a north-to-south younging trend ranging from 24 to 8 Ma. Thus, the diachronous break-off events of the SIL and the resultant rupturing of the continental lithosphere have important implications for the driving force of these post-collisional geological processes across the Tibetan Plateau. Based on the compiled age spectra (Fig. 1B), the latter break-off event (26 Ma for 80°E–85°E and 23 Ma for 85°E–90°E) started earlier (7–8 Ma) than the cessation of the former event (19 Ma for 74°E–79°E and 15 Ma for 80°E–85°E). We propose that this feature is most likely due to the northward depression of the asthenosphere underlying the SIL. This mobile asthenosphere first advected through the weakened portions of the overriding Indian lithosphere at the WHS and EHS at ca. 33 and 30 Ma, respectively, and then through the other two tears (26 Ma for 80°E and 23 Ma for 86°E) in the central part of the Lhasa terrane (Fig. 12). It induced diachronous foundering associated with upward bending of the Indian slab, further accelerating the tearing of the SIL during continental subduction. The northward flow and the rebounding of the SIL may have significantly facilitated the lithosphere deformation and uplift of the Tibetan Plateau.

CONCLUSION

The distribution of Oligo–Miocene magmatic rocks from southern Tibet in space and time yields critical information on the geometry and deformation of the SIL which impacted plateau growth following the collision between India and Eurasia. Here we report variations in the crystallization ages and temperatures of these post-collisional magmatic rocks, demonstrating that (1) timing of these rocks exhibits four patterns of decreasing ages approximately corresponding to the torn SIL and (2) contrasting trends in mineral crystallization temperatures and decreasing melting source depth recorded in the ultrapotassic-potassic magmas corresponding spatially to regions of slab window and flattened subducted lithosphere as recorded by seismic tomography. These data sets together imply that the focused mantle flow may advance diachronously through pre-existing weakened sectors within the overlying SIL. It could induce diachronous foundering, associated with the upward bending of the Indian slab, which consequently led to the tearing of the SIL during continental subduction.

ACKNOWLEDGMENTS

This research is supported by the National Natural Science Foundation of China (grant no. 41730211), the Second Tibetan Plateau Scientific Expedition and Research Program (2019QZKK0702), and Public Welfare Basic Research of Zhejiang Province (no. LGF20D020001). We thank X. Song and J. Li for sharing their regional shear-wave tomographic model. We thank Yuan-Bao Wu, Oliver Jagoutz, and Yaoling Niu for their helpful discussion and improving the paper.

REFERENCES CITED

Bian, S., Gong, J.F., Zuza, A.V., Yang, R., Tian, Y.T., Ji, J.Q., Chen, H.L., Xu, Q.Q., Chen, L., Lin, X.B., Cheng, X.G., Tu, J.Y., and Yu, X.J., 2020, Late Pliocene onset of the Cona rift, eastern Himalaya, confirms eastward propagation of extension in Himalayan-Tibetan orogen: Earth and Planetary Science Letters, v. 544, https://doi.org/10.1016/j.epsl.2020.116383.

Bird, P., 1978, Initiation of intracontinental subduction in the Himalaya: Journal of Geophysical Research, v. 83, no. B10, p. 4975–4987, https://doi.org/10.1029/JB083iB10p04975.

Blisniuk, P.M., Hacker, B.R., Glodny, J., Ratschbacher, L., Bi, S.W., Wu, Z.H., McWilliams, M.O., and Calvert, A., 2001, Normal faulting in central Tibet since at least 13.5 Myr ago: Nature, v. 412, p. 628–632, https://doi.org/10.1038/35088045.

Chen, M., Niu, F., Tromp, J., Lenardic, A., Lee, C., Cao, W., and Ribeiro, J., 2017, Lithospheric foundering and underthrusting imaged beneath Tibet: Nature Communications, v. 8, https://doi.org/10.1038/ncomms15659.

Chen, Y., Li, W., Yuan, X., Badal, J., and Teng, J., 2015, Tearing of the Indian lithospheric slab beneath southern Tibet revealed by SKS-wave splitting measurements: Earth and Planetary Science Letters, v. 413, p. 13–24, https://doi.org/10.1016/j.epsl.2014.12.041.

Chung, S.-L., Liu, D., Ji, J., Chu, M.-F., Lee, H.-Y., Wen, D.-J., Lo, C.-H., Lee, T.-Y., Qian, Q., and Zhang, Q., 2003, Adakites from continental collision zones: Melting of thickened lower crust beneath southern Tibet: Geology, v. 31, no. 11, p. 1021–1024, https://doi.org/10.1130/G19796.1.

Chung, S.-L., Chu, M.-F., Zhang, Y., Xie, Y., Lo, C.-H., Lee, T.-Y., Lan, C.-Y., Li, X., Zhang, Q., and Wang, Y., 2005, Tibetan tectonic evolution inferred from spatial and temporal variations in post-collisional magmatism: Earth-Science Reviews, v. 68, no. 3-4, p. 173–196, https://doi.org/10.1016/j.earscirev.2004.05.001.

Coleman, M., and Hodges, K., 1995, Evidence for Tibetan plateau uplift before 14 Myr ago from a new minimum age for east-west extension: Nature, v. 374, p. 49–52, https://doi.org/10.1038/374049a0.

Coulon, C., Maluski, H., Bollinger, C., and Wang, S., 1986, Mesozoic and Cenozoic volcanic rocks from central and southern Tibet: ^{39}Ar-^{40}Ar dating, petrological characteristics and geodynamical significance: Earth and Planetary Science Letters, v. 79, no. 3–4, p. 281–302, https://doi.org/10.1016/0012-821X(86)90186-X.

Dai, H., Zheng, J., Griffin, W., O'Reilly, S., Xiong, Q., Ping, X., Chen, F., and Lu, J., 2021, Pyroxenite xenoliths record complex melt impregnation in the deep lithosphere of the northwestern North China Craton: Journal of Petrology, v. 62, no. 2, p. 1–32, https://doi.org/10.1093/petrology/egaa079.

Dasgupta, R., Jackson, M.G., and Lee, C.T., 2010, Major element chemistry of ocean island basalts: conditions of mantle melting and heterogeneity of mantle source: Earth and Planetary Science Letters, v. 289, p. 377–392, https://doi.org/10.1016/j.epsl.2009.11.027.

Davies, J.H., and von Blanckenburg, F., 1995, Slab breakoff: A model of lithosphere detachment and its test in the magmatism and deformation of collisional orogens: Earth and Planetary Science Letters, v. 129, no. 1–4, p. 85–102, https://doi.org/10.1016/0012-821X(94)00237-S.

Dewey, F., 1988, Extensional collapse of orogens: Tectonics, v. 7, p. 1123–1139, https://doi.org/10.1029/TC007i006p01123.

Dilek, Y., and Sandvol, E., 2009, Seismic structure, crustal architecture and tectonic evolution of the Anatolian-African plate boundary and the Cenozoic orogenic belts in the eastern Mediterranean region, *in* Murphy, J.B., Keppie, J.D., and Hynes, A.J., eds., Ancient Orogens and Modern Analogues: Geological Society, London, Special Publication 327, p. 127–160, https://doi.org/10.1144/SP327.8.

Ding, L., Kapp, P., Yue, Y., and Lai, Q., 2007, Postcollisional calc-alkaline lavas and xenoliths from the southern Qiangtang terrane, central Tibet: Earth and Planetary Science Letters, v. 254, no. 1–2, p. 28–38, https://doi.org/10.1016/j.epsl.2006.11.019.

Ferry, J., and Watson, E., 2007, New thermodynamic models and revised calibrations for the Ti-in-zircon and Zr-in-rutile thermometers: Contributions to Mineralogy and Petrology, v. 154, no. 4, p. 429–437, https://doi.org/10.1007/s00410-007-0201-0.

Gao, R., Lu, Z., Klemperer, S.L., Wang, H., Dong, S., Li, W., and Li, H., 2016, Crustal-scale duplexing beneath the Yarlung Zangbo suture in the western Himalaya: Nature Geoscience, v. 9, no. 7, p. 555–560, https://doi.org/10.1038/ngeo2730.

Gilotti, J.A., 2013, The realm of ultrahigh-pressure metamorphism: Elements, v. 9, no. 4, p. 255–260, https://doi.org/10.2113/gselements.9.4.255.

Green, D.H., and Ringwood, A.E., 1967, The genesis of basaltic magmas: Contributions to Mineralogy and Petrology, v. 15, p. 103–190, https://doi.org/10.1007/BF00372052.

Guo, Z., Wilson, M., Zhang, M., Cheng, Z., and Zhang, L., 2015, Post-collisional ultrapotassic mafic magmatism in South Tibet: Products of partial melting of pyroxenite in the mantle wedge induced by roll-back and delamination of the subducted Indian continental lithosphere slab: Journal of Petrology, v. 56, no. 7, p. 1365–1406, https://doi.org/10.1093/petrology/egv040.

Guo, Z.F., and Wilson, M., 2019, Late Oligocene–early Miocene transformation of postcollisional magmatism in Tibet: Geology, v. 47, no. 8, p. 776–780, https://doi.org/10.1130/G46147.1.

Guo, Z.F., Wilson, M., Zhang, M.L., Cheng, Z.H., and Zhang, L.H., 2013, Post-collisional, K-rich mafic magmatism in South Tibet: Constraints on Indian slab-to-wedge transport processes and plateau uplift: Contributions to Mineralogy and Petrology, v. 165, p. 1311–1340, https://doi.org/10.1007/s00410-013-0860-y.

Hao, L., Wang, Q., Kerr, A., Yang, J., Ma, L., Qi, Y., Wang, J., and Ou, Q., 2021, Post-collisional crustal thickening and plateau uplift of southern Tibet: Insights from

Cenozoic magmatism in the Wuyu area of the eastern Lhasa block: Geological Society of America Bulletin, v. 133, no. 7–8, p. 1634–1648, https://doi.org/10.1130/B35659.1.

Hao, L., Wang, Q., Kerr, A., Wei, G., Huang, F., Zhang, M., Qi, Y., Ma, L., Chen, X., and Yang, Y., 2022, Contribution of continental subduction to very light B isotope signatures in post-collisional magmas: Evidence from southern Tibetan ultrapotassic rocks: Earth and Planetary Science Letters, v. 584, https://doi.org/10.1016/j.epsl.2022.117508.

Herzberg, C.T., 2011, Identification of source lithology in the Hawaiian and Canary Islands: implication for origins: Journal of Petrology, v. 52, p. 113–146, https://doi.org/10.1093/petrology/egq075.

Hildebrand, R.S., Whalen, J.B., and Bowring, S.A., 2018, Resolving the crustal composition paradox by 3.8 billion years of slab failure magmatism and collisional recycling of continental crust: Tectonophysics, v. 734–735, p. 69–88, https://doi.org/10.1016/j.tecto.2018.04.001.

Hou, Z.Q., Gao, Y.F., Qu, X.M., Rui, Z.Y., and Mo, X.X., 2004, Origin of adakitic intrusives generated during mid-Miocene east-west extension in southern Tibet: Earth and Planetary Science Letters, v. 220, no. 1–2, p. 139–155, https://doi.org/10.1016/S0012-821X(04)00007-X.

Kosarev, G., Kind, R., Sobolev, S., Yuan, X., Hanka, W., and Oreshin, S., 1999, Seismic evidence for a detached Indian lithospheric mantle beneath Tibet: Science, v. 283, no. 5406, p. 1306–1309, https://doi.org/10.1126/science.283.5406.1306.

Kufner, S., Kakar, N., Bezada, M., Bloch, W., Metzger, S., Yuan, X., Mechie, J., Ratschbacher, L., Murodkulov, S., Deng, Z., and Schurr, B., 2021, The Hindu Kush slab break-off as revealed by deep structure and crustal deformation: Nature Communications, v. 12, 1685, https://doi.org/10.1038/s41467-021-21760-w.

Kusky, T.M., 1993, Collapse of Archean orogens and the generation of late-to post-kinematic granitoids: Geology, v. 21, no. 10, p. 925–928, https://doi.org/10.1130/0091-7613(1993)021<0925:COAOAT>2.3.CO;2.

Kusky, T.M., and Wang, L., 2022, Growth of continental crust in intra-oceanic and continental margin arc systems: Analogs for Archean systems: Science China: Earth Sciences, https://doi.org/10.1007/s11430-021-9964-1.

Kusky, T.M., Windley, B.F., Polat, A., Wang, L., Ning, W.B., and Zhong, Y.T., 2021, Archean dome-and-basin style structures form during growth of intraoceanic and continental-margin arcs and their death by slab failure and collision: Earth-Science Reviews, v. 220, https://doi.org/10.1016/j.earscirev.2021.103725.

Lambart, S., Laporte, D., and Schiano, P., 2013, Markers of the pyroxenite contribution in the major-element compositions of oceanic basalts: Review of experimental constraints: Lithos, v. 160–161, p. 14–36, https://doi.org/10.1016/j.lithos.2012.11.018.

Lanari, P., Riel, N., Guillot, S., Vidal, O., Schwartz, S., Pêcher, A., and Hattori, K.H., 2013, Deciphering high-pressure metamorphism in collisional context using microprobe mapping methods: Application to the Stak eclogitic massif (northwest Himalaya): Geology, v. 41, no. 2, p. 111–114, https://doi.org/10.1130/G33523.1.

Li, J., and Song, X., 2018, Tearing of Indian mantle lithosphere from high-resolution seismic images and its implications for lithosphere coupling in southern Tibet: Proceedings of the National Academy of Sciences of the United States of America, v. 115, no. 33, p. 8296–8300, https://doi.org/10.1073/pnas.1717258115.

Liang, X., Chen, Y., Tian, X., Chen, Y.J., Ni, J., Gallegos, A., Klemperer, S.L., Wang, M., Xu, T., and Sun, C., 2016, 3D imaging of subducting and fragmenting Indian continental lithosphere beneath southern and central Tibet using body-wave finite-frequency tomography: Earth and Planetary Science Letters, v. 443, p. 162–175, https://doi.org/10.1016/j.epsl.2016.03.029.

Liu, D., Zhao, Z., Zhu, D., Niu, Y., and Harrison, T.M., 2014, Zircon xenocrysts in Tibetan ultrapotassic magmas: Imaging the deep crust through time: Geology, v. 42, no. 1, p. 43–46, https://doi.org/10.1130/G34902.1.

Liu, Y., Gao, S., Hu, Z., Gao, C., Zong, K., and Wang, D., 2010, Continental and oceanic crust recycling-induced melt-peridotite interactions in the Trans-North China Orogen: U-Pb dating, Hf isotopes and trace elements in zircons from mantle xenoliths: Journal of Petrology, v. 51, no. 1–2, p. 537–571, https://doi.org/10.1093/petrology/egp082.

Liu, Z., Tian, X.B., Yuan, X.H., Liang, X.F., Chen, Y., Zhu, G.H., Zhang, H.S., Li, W., Tan, P., Zuo, S.C., Wu, C.L., Nie, S.T., Wang, G.C., Yu, G.P., and Zhou, B.B., 2020, Complex structure of upper mantle beneath the Yadong-Gulu rift in Tibet revealed by S-to-P converted waves: Earth and Planetary Science Letters, v. 531, https://doi.org/10.1016/j.epsl.2019.115954.

Ludwig, K., 2003, User's manual for Isoplot 3.00: A geochronological toolkit for Microsoft Excel: Berkely Geochronology Center Special Publication 4, 70 p.

Ma, Q., Zheng, J., Griffin, W.L., Zhang, M., Tang, H., Su, Y., and Ping, X., 2012, Triassic "adakitic" rocks in an extensional setting (North China): Melts from the cratonic lower crust: Lithos, v. 149, p. 159–173, https://doi.org/10.1016/j.lithos.2012.04.017.

Magni, V., Allen, M.B., van Hunen, J., and Bouilhol, P., 2017, Continental underplating after slab break-off: Earth and Planetary Science Letters, v. 474, p. 59–67, https://doi.org/10.1016/j.epsl.2017.06.017.

Mahéo, G., Guillot, S., Blichert-Toft, J., Rolland, Y., and Pecher, A., 2002, A slab breakoff model for the Neogene thermal evolution of South Karakorum and South Tibet: Earth and Planetary Science Letters, v. 195, no. 1–2, p. 45–58, https://doi.org/10.1016/S0012-821X(01)00578-7.

Miller, C., Schuster, R., Klötzli, U., Frank, W., and Purtscheller, F., 1999, Post-collisional potassic and ultrapotassic magmatism in SW Tibet: Geochemical and Sr-Nd-Pb-O isotopic constraints for mantle source characteristics and petrogenesis: Journal of Petrology, v. 40, no. 9, p. 1399–1424, https://doi.org/10.1093/petroj/40.9.1399.

Mitsuishi, M., Wallis, S.R., Aoya, M., Lee, J., and Wang, Y., 2012, E–W extension at 19 Ma in the Kung Co area, S. Tibet: Evidence for contemporaneous E–W and N–S extension in the Himalayan orogen: Earth and Planetary Science Letters, v. 325–326, p. 10–20, https://doi.org/10.1016/j.epsl.2011.11.013.

Molnar, P., England, P., and Martinod, J., 1993, Mantle dynamics, uplift of the Tibetan Plateau, and the Indian monsoon: Reviews of Geophysics, v. 31, no. 4, p. 357–396, https://doi.org/10.1029/93RG02030.

Neave, D.A., and Putirka, K.D., 2017, A new clinopyroxene-liquid barometer, and implications for magma storage pressures under Icelandic rift zones: The American Mineralogist, v. 102, p. 777–794, https://doi.org/10.2138/am-2017-5968.

Nomade, S., Renne, P.R., Mo, X.X., Zhao, Z.D., and Zhou, S., 2004, Miocene volcanism in the Lhasa block, Tibet: Spatial trends and geodynamic implications: Earth and Planetary Science Letters, v. 221, no. 1–4, p. 227–243, https://doi.org/10.1016/S0012-821X(04)00072-X.

Pan, F.-B., Zhang, H.-F., Harris, N., Xu, W.-C., and Guo, L., 2012, Oligocene magmatism in the eastern margin of the east Himalayan syntaxis and its implication for the India–Asia post-collisional process: Lithos, v. 154, p. 181–192, https://doi.org/10.1016/j.lithos.2012.07.004.

Putirka, K., 2008, Thermometers and barometers for volcanic systems: Reviews in Mineralogy and Geochemistry, v. 69, no. 1, p. 61–120, https://doi.org/10.2138/rmg.2008.69.3.

Schulte-Pelkum, V., Monsalve, G., Sheehan, A., Pandey, M., Sapkota, S., Bilham, R., and Wu, F., 2005, Imaging the Indian subcontinent beneath the Himalaya: Nature, v. 435, p. 1222–1225, https://doi.org/10.1038/nature03678.

Searle, M.P., Windley, B.F., Coward, M.P., Cooper, D.J.W., Rex, A.J., Rex, D., Li, T.D., Xiao, X.C., Jan, M.Q., Thakur, V.C., and Kumar, S., 1987, The closing of Tethys and the tectonics of the Himalaya: Geological Society of America Bulletin, v. 98, no. 6, p. 678–701, https://doi.org/10.1130/0016-7606(1987)98<678:TCOTAT>2.0.CO;2.

Shi, D., Klemperer, S.L., Shi, J., Wu, Z., and Zhao, W., 2020, Localized foundering of Indian lower crust in the India–Tibet collision zone: Proceedings of the National Academy of Sciences of the United States of America, v. 117, no. 40, p. 24742–24747, https://doi.org/10.1073/pnas.2000015117.

Sun, S.-s., and McDonough, W.F., 1989, Chemical and isotopic systematics of oceanic basalts: Implications for mantle composition and processes, *in* Saunders, A.D., and Norry, M.J., eds., Magmatism in the Ocean Basins: Geological Society, London, Special Publication 42, p. 313–345, https://doi.org/10.1144/GSL.SP.1989.042.01.19.

Sun, X., Lu, Y.J., McCuaig, T.C., Zheng, Y.Y., Chang, H.F., Guo, F., and Xu, L.J., 2018, Miocene ultrapotassic, high-Mg dioritic, and adakite-like rocks from Zhunuo in southern Tibet: Implications for mantle metasomatism and porphyry copper mineralization in collisional orogens: Journal of Petrology, v. 59, p. 341–386, https://doi.org/10.1093/petrology/egy028.

Tilmann, F., Ni, J, and the Indepth III Seismic Team, 2003, Seismic imaging of the downwelling Indian lithosphere beneath central Tibet: Science, v. 300, no. 5624, p. 1424–1427, https://doi.org/10.1126/science.1082777.

Turner, S., Hawkesworth, C., Liu, J., Rogers, N., Kelley, S., and Van Calsteren, P., 1993, Timing of Tibetan uplift constrained by analysis of volcanic rocks: Nature, v. 364, p. 50–54, https://doi.org/10.1038/364050a0.

Turner, S., Arnaud, N.O., Liu, J., Rogers, N.W., Hawkesworth, C.J., Harris, N., Kelley, S.P., Van Calsteren, P., and Deng, W., 1996, Post-collision, Shoshonitic volcanism on the Tibetan Plateau: Implications for convective thinning of the lithosphere and the source of ocean island basalts: Journal of Petrology, v. 37, no. 1, p. 45–71, https://doi.org/10.1093/petrology/37.1.45.

van Hinsbergen, D.J., Steinberger, B., Doubrovine, P.V., and Gassmöller, R., 2011, Acceleration and deceleration of India-Asia convergence since the Cretaceous: Roles of mantle plumes and continental collision: Journal of Geophysical Research: Solid Earth, v. 116, no. B6, https://doi.org/10.1029/2010JB008051.

Walter, M.J., 1998, Melting of garnet peridotite and the origin of kamatiite and depleted lithosphere: Journal of Petrology, v. 39, p. 29–60, https://doi.org/10.1093/petroj/39.1.29.

Wang, R., Roberto, W., Zhu, D.C., Hou, Z.Q., and Yang, Z.M., 2022, The impact of a tear in the subducted Indian plate on the Miocene geology of the Himalayan-Tibetan orogen: Geological Society of America Bulletin, v. 134, no. 3–4, p. 681–690, https://doi.org/10.1130/B36023.1.

Webb, A., Guo, H., Clift, P., Husson, L., Müller, T., Costantino, D., Yin, A., Xu, Z., Cao, H., and Wang, Q., 2017, The Himalaya in 3D: Slab dynamics controlled mountain building and monsoon intensification: Lithosphere, v. 9, p. 637–651, https://doi.org/10.1130/L636.1.

Whitney, L., Teyssier, C., Rey, P., and Buck, R., 2013, Continental and oceanic core complexes: Geological Society of America Bulletin, v. 125, no. 3–4, p. 273–298, https://doi.org/10.1130/B30754.1.

Wiedenbeck, M., Allé, P., Corfu, F., Griffin, W.L., Meier, M., Oberli, F., Von Quadt, A., Roddick, J.C., and Spiegel, W., 1995, Three natural zircon standards for U-Th-Pb, Lu-Hf, trace element and REE analyses: Geostandards Newsletter, v. 19, no. 1, p. 1–23, https://doi.org/10.1111/j.1751-908X.1995.tb00147.x.

Williams, H., Turner, S., Kelley, S., and Harris, N., 2001, Age and composition of dikes in Southern Tibet: New constraints on the timing of east-west extension and its relationship to postcollisional volcanism: Geology, v. 29, no. 4, p. 339–342, https://doi.org/10.1130/0091-7613(2001)029<0339:AACODI>2.0.CO;2.

Williams, H.M., Turner, S.P., Pearce, J.A., Kelley, S., and Harris, N., 2004, Nature of the source regions for post-collisional, potassic magmatism in southern and northern Tibet from geochemical variations and inverse trace element modelling: Journal of Petrology, v. 45, no. 3, p. 555–607, https://doi.org/10.1093/petrology/egg094.

Wilson, M., and Bianchini, G., 1999, Tertiary-Quaternary magmatism within the Mediterranean and surrounding region, *in* Durand, B., Jolivet, L., Horváth, F., and Séranne, M., eds., The Mediterranean Basins: Tertiary Extension within the Alpine Orogen: Geological Society, London, Special Publication 156, p. 141–168, https://doi.org/10.1144/GSL.SP.1999.156.01.09.

Wu, Y., Bao, X., Zhang, B., Xu, Y., and Yang, W., 2022, Seismic evidence for stepwise lithospheric delamination beneath the Tibetan Plateau: Geophysical Research Letters, v. 49, https://doi.org/10.1029/2022GL098528.

Ye, K., Cong, B.L., and Ye, D.N., 2000, The possible subduction of continental materials to depths greater than 200 km: Nature, v. 407, p. 734–736, https://doi.org/10.1038/35037566.

Zhang, H., Harris, N., Parrish, R., Kelley, S., Zhang, L., Rogers, N., Argles, T., and King, J., 2004, Causes and consequences of protracted melting of the mid-crust exposed in the North Himalayan antiform: Earth and Planetary Science Letters, v. 228, no. 1–2, p. 195–212, https://doi.org/10.1016/j.epsl.2004.09.031.

Zhang, J., Liu, Y., Ling, W., and Gao, S., 2017a, Pressure-dependent compatibility of iron in garnet: Insights into the origin of ferropicritic melt: Geochimica et Cosmochimica Acta, v. 197, p. 356–377, https://doi.org/10.1016/j.gca.2016.10.047.

Zhang, L.H., Guo, Z.F., Zhang, M.L., Cheng, Z.H., and Sun, Y.T., 2017b, Post-collisional potassic magmatism in the eastern Lhasa terrane, South Tibet: Products of partial melting of mélanges in a continental subduction channel: Gondwana Research, v. 41, p. 9–28, https://doi.org/10.1016/j.gr.2015.11.007.

Zhang, L.-Y., Ducea, M.N., Ding, L., Pullen, A., Kapp, P., and Hoffman, D., 2014, Southern Tibetan Oligocene–Miocene adakites: A record of Indian slab tearing: Lithos, v. 210-211, p. 209–223, https://doi.org/10.1016/j.lithos.2014.09.029.

Zhao, L., Paul, A., Guillot, S., Solarino, S., Malusa, M.G., Zheng, T.Y., Aubert, C., Salimbeni, S., Dumont, T., Schwartz, S., Zhu, R.X., and Wang, Q.C., 2015, First seismic evidence for continental subduction beneath the Western Alps: Geology, v. 43, no. 9, p. 815–818, https://doi.org/10.1130/G36833.1.

Zhao, Z., Mo, X., Dilek, Y., Niu, Y., DePaolo, D.J., Robinson, P., Zhu, D., Sun, C., Dong, G., and Zhou, S., 2009, Geochemical and Sr-Nd-Pb-O isotopic compositions of the post-collisional ultrapotassic magmatism in SW Tibet: Petrogenesis and implications for India intracontinental subduction beneath southern Tibet: Lithos, v. 113, no. 1–2, p. 190–212, https://doi.org/10.1016/j.lithos.2009.02.004.

Zheng, Y.-F., Chen, Y.-X., Chen, R.-X., and Dai, L.-Q., 2022, Tectonic evolution of convergent plate margins and its geological effects: Science China: Earth Sciences, v. 65, https://doi.org/10.1007/s11430-022-9947-6.

Zhu, D., Wang, Q., Chung, S., Cawood, P.A., and Zhao, Z., 2019, Gangdese magmatism in southern Tibet and India-Asia convergence since 120 Ma, *in* Treloar, P.J., and Searle, M.P., eds., Himalayan Tectonics: A Modern Synthesis: Geological Society, London, Special Publication 483, p. 583–604, https://doi.org/10.1144/SP483.14.

Science Editor: Brad Singer
Associate Editor: Emily Finzel

Manuscript Received 31 August 2022
Revised Manuscript Received 12 December 2022
Manuscript Accepted 10 February 2023

Printed in the USA